INTERNATIONAL JOURNAL OF REMOTE SENSING
2019, VOL. 40, NO. 2, 532–554
https://doi.org/10.1080/01431161.2018.1514542

Taylor & Francis
Taylor & Francis Group

Coseismic deformation and source model of the 12 November 2017 M_W 7.3 Kermanshah Earthquake (Iran–Iraq border) investigated through DInSAR measurements

Jianming Kuang[a], Linlin Ge [a], Graciela Isabel Metternicht[b], Alex Hay-Man Ng[a,c], Hua Wang[c], Mehdi Zare[d] and Farnaz Kamranzad[e]

[a]Geoscience and Earth Observing Systems Group (GEOS), School of Civil and Environmental Engineering, The University of New South Wales (UNSW), Sydney, Australia; [b]School of Biological, Earth and Environmental Sciences, The University of New South Wales (UNSW), Sydney, Australia; [c]Department of Surveying Engineering, Guangdong University of Technology, Guangzhou, China; [d]Engineering Seismology Department, International Institute of Earthquake Engineering and Seismology (IIEES), Tehran, Iran; [e]Geo-Engineering Laboratory, College of Engineering, University of Tehran, Tehran, Iran

ABSTRACT

A large earthquake with a magnitude of M_W 7.3 struck the border of Iran and Iraq at the province of Kermanshah, Iran. In our study, coseismic deformation and source model of the 12 November 2017 Kermanshah Earthquake are investigated using ALOS-2 ScanSAR and Sentinel-1A/B TOPSAR Differential Interferometric Synthetic Aperture Radar (DInSAR) techniques. Geodetic inversion has been performed to constrain source parameters and invert slip distribution on the fault plane. The optimised source model from joint inversion shows a blind reverse fault with a relatively large right-lateral component, striking 353.5° NNW-SSE and dipping 16.3° NE. The maximum slip is up to 3.8 m at 12–14 km depth and the inferred seismic moment is 1.01×10^{20} Nm, corresponding to M_W 7.3, consistent with seismological solutions. The high-resolution optical images from SuperView-1 satellite suggest that most of the linear surface features mapped by DInSAR measurements are landslides or surface cracks triggered by the earthquake. Coulomb stress changes on the source fault indicating consistency between aftershock distribution and high loaded stress zones. Based on the stress change on neighbouring active faults around this area, the Kermanshah Earthquake has brought two segments of the Zagros Mountain Front Fault (MFF), MFF-1 and MFF-2, 0.5–3.1 MPa and 0.5–1.96 MPa closer to failure, respectively, suggesting the risk of future earthquakes. Recent major aftershocks ($M_W \geq 5.0$) could probably ease the seismic hazard on MFF-2, but the risk of earthquakes on MFF-2 is still increasing.

ARTICLE HISTORY
Received 13 May 2018
Accepted 17 August 2018

CONTACT Linlin Ge l.ge@unsw.edu.au the University of New South Wales, Civil Engineering Building (H20), Level 4, Room CE414, Kensington Campus, 2052 Sydney, NSW, Australia

1. Introduction

1.1. *The 12 November 2017 Kermanshah earthquake*

On 12 November 2017, an M_W 7.3 earthquake struck the border region between Iran and Iraq, causing severe infrastructure damage over large areas with more than 620 fatalities and 8100 people injured. According to the United States Geological Survey (USGS), the epicentre was located at 34.905°N and 45.956°E with a depth of 19 km (United States Geological Survey 2017). A significant foreshock with a magnitude of 4.4 occurred about one hour before the main shock, located just 60 km SW of the main shock. Aftershocks with M_W> 2.5, as collected from the Iranian Seismological Centre (IRSC) between 12 November 2017 and 15 April 2018 suggest that the epicentre zone covered an area of approximately 100 km× 80 km (Figure 1). The epicentre location and moment magnitude of this event were also determined by the strong motion data of 109 stations from the Iran Strong Motion Network (ISMN), indicating a magnitude of 7.3 occurred at a depth of 18.0 km (Farzanegan et al. 2017). Focal mechanism resolved by seismological

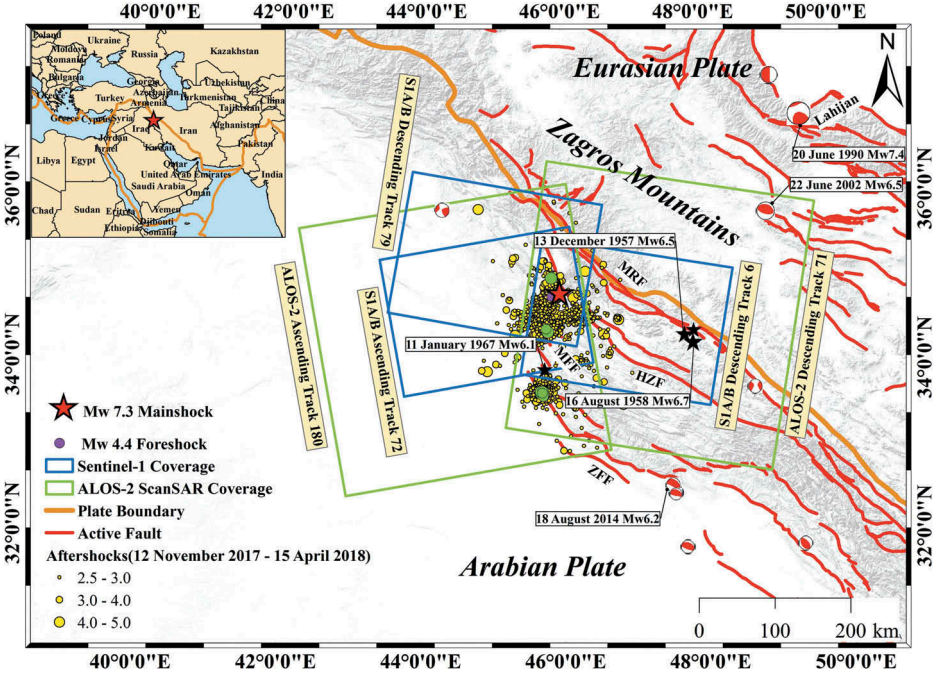

Figure 1. Tectonic setting of the 2017 M_W 7.3 Kermanshah Earthquake. Red star is the main shock and violet circle is the foreshock. Yellow circles are aftershocks with 2.5 < M_W < 5.0 occurred between 12 November 2017 and 15 April 2018 collected from Iranian Seismological Centre (IRSC). Green circles are major events with M_W > 5.0 after the main shock. Red lines are active faults from International Institute of Earthquake Engineering and Seismology (IIEES) (Hessami, Jamali, and Tabassi 2003) with the Zagros Main Recent Fault (MRF), the High Zagros Fault (HZF), the Zagros Mountain Front Fault (MFF) and the Zagros Foredeep Fault (ZFF). Brown line indicates the plate boundary. Green and blue boxes represent the spatial coverage of ALOS-2 and Sentinel-1A/B SAR image pairs, respectively. Black stars represent the major historical earthquakes with M_W > 6.0 before 1976 from USGS. Red focal mechanism plots denote the historical earthquakes with M_W > 6.0 between 1976 and 2014 from GCMT.

data from the USGS and the Global Centroid Moment Tensor (GCMT) (Dziewonski, Chou, and Woodhouse 1981) both show a coseismic rupture occurred on a NNW-SSE strike, oblique-thrust fault.

Preliminary field investigation carried out by the International Institute of Earthquake Engineering and Seismology (IIEES) reveals that the Sarpol Zahab and Qasr Shirin cities of Kermanshah Province in Iran suffered the most serious destruction and the maximum intensities (Zare et al. 2017). In addition, a preliminary assessment conducted by the Geological Survey of Iran also shows many local photos of the secondary coseismic geological features on the ground, including landslide-rock avalanche, rockfalls, and cracks on the Sarpol Zahab region and Ezgaleh city (Shahryar Solaymani Azad et al. 2017). According to the News report from the Nalia Radio and Television (NRT), the Darbandikhan Dam, a multi-purpose embankment located in the city of Darbandikhan, has suffered a 450 m long crack in the upper part of the dam. The field survey carried by Building & Housing Research Centre (BHRC) also shows that there were many surface ruptures over the city of Sarpol Zahab, with a vertical displacement up to 3 m, and a width of rupture reaching 1 km. Hence, this paper aims to further investigate whether most of the surface ruptures and cracks around the epicentre area were due to secondary fault ruptures, or triggered by gravitational deformation and cracks.

1.2. *Tectonic background*

The epicentre of the 2017 Kermanshah Earthquake is close to the Zagros Mountains originated by the northward collision between Eurasian plate and Arabian plate with a rate of approximately 20 mm year^{-1} (Reilinger et al. 1997; Mouthereau, Lacombe, and Vergés 2012; Madanipour et al. 2013). These two plates converge at the Main Recent Fault and Main Zagros Reverse Fault which both bounded the Zagros fold and thrust belt (McQuarrie 2004). The active faults in this region are mostly trending NW-SE, NNW-SSE with dips of 30–60° and rakes of 60–120° along the plate boundary (Hessami, Jamali, and Tabassi 2003). The Zagros Main Recent Fault (MRF), the High Zagros Fault (HZF), the Zagros Mountain Front Fault (MFF) and the Zagros Foredeep Fault (ZFF) are major faults in this region, as shown in Figure 1.

Even though this event is located close to the compressional boundary between two major plates, fewer large historical earthquakes have been recorded around this region. Historical earthquakes with M_W> 6.0 within 400 km of the main shock recorded by the USGS before 1976, and the GCMT from 1976 to 2014, indicate a low rate of seismicity background for this region. A total of 13 previous earthquakes with M_W> 6.0 occurred in this region, and only two of them had a magnitude of over 6.5. The nearest one, recorded at a magnitude of 6.1, occurred on 11 January 1967 on the MFF, located about 100 km south of the 2017 Kermanshah Earthquake. The earliest recorded earthquake (M_W 6.5) struck on the MRF on 13 December 1957, followed by another two major earthquakes with a peak magnitude of 6.7 in 1958 in the same area, about 190 km SE of the Kermanshah Earthquake. A field investigation of this earliest reported earthquake shows an area of over 2800 km^2 was damaged, and nearly 1200 lives were lost (Ambraseys, Moinfar, and Peronaci 1973). However, the most serious and largest historical earthquake around this region was recorded on 20 June 1990; located around 400 km NE of the Kermanshah earthquake zone, on the Lahijan Fault, this quake of a

magnitude of 7.4 (M_W) caused over 40,000 fatalities and 60,000 injuries, leaving 500,000 people homeless (Berberian et al. 1992). The most recent historical event was reported on the SE segments of the MFF on 18 August 2014 (M_W 6.2), approximately 290 km SE of the 2017 Kermanshah Earthquake. Owing to fewer major earthquakes and lack of GPS stations installed in this region, the local strain around the plate boundary was not accurately estimated by seismological or geodetic data (Kreemer, Blewitt, and Klein 2014). However, the 2017 Kermanshah Earthquake provides researchers an opportunity to assess the risk of seismic hazard around this region using remote sensing data.

Hence, this study is set to measure the 2017 Kermanshah Earthquake-induced coseismic deformation using the ALOS-2 ScanSAR and Sentinel-1A/B TOPSAR data. The source model and slip distribution of the event were determined from a joint inversion of DInSAR measurements based on an elastic dislocation model (Okada 1985). High-resolution optical images from SuperView-1 and DInSAR wrapped interferograms were used to investigate the linear surface features mapped by DInSAR measurements. In addition, coseismic Coulomb stress changes on the source fault and neighbouring active faults were explored to understand the stress change between aftershock distribution and different fault planes. The triggering relationship between most recent events (M_W> 5.0) and stress changes on different fault planes was further explored. We aim to demonstrate that remote sensing data, either radar or optical data, can play an important role in earthquake monitoring and natural hazard response in regions of scarce ground survey data.

2. Data availability and DInSAR measurements

2.1. *Data availability*

The dataset for this study consist of two SAR image pairs from ALOS-2 satellite (L-band) operated by the Japan Aerospace Exploration Agency (JAXA) and three pairs from Sentinel-1A/B (C-band) operated under the Copernicus program from the European Space Agency (ESA). Table 1 provides detailed information for each pair of images, and Figure 1 shows their spatial coverage.

The wavelengths of Sentinel-1A/B and ALOS-2 data are 5.6 cm and 22.9 cm, respectively. The Sentinel-1A/B image pairs were acquired in Terrain Observation by Progressive Scans (TOPS) mode. TOPS SAR data can cover a swath width of 250 km at about 5 m by 20 m resolution in the range and azimuth directions, respectively (Torres et al. 2012; De Zan and Monti Guarnieri 2006). The ALOS-2 image pairs used were acquired in the ScanSAR (Wide Swath) mode with a swath of 350 km. Two pairs of descending Sentinel-1A/B data were needed to fully cover the area of interest. Because of the low vegetation and desert-like

Table 1. SAR image pairs used in this study.

Satellite	Track	Orbit	Image Mode	Master (dd mm yyyy)	Slave (dd mm yyyy)	$B_\perp$(m)	B_T(day)	θ(°)
ALOS-2	180	ASC	WD	9 August 2016	14 November 2017	−86	462	40
	71	DESC	WD	4 October 2017	15 November 2017	167	42	40
Sentinel-1A/B	72	ASC	IWS	11 November 2017	17 November 2017	62	6	39
	79	DESC	IWS	12 November 2017	18 November 2017	56	6	39
	6	DESC	IWS	7 November 2017	19 November 2017	15	12	39

ASC is ascending and DESC is descending path. WD is Wide-Swath (ScanSAR) mode and IWS is Interferometric Wide Swath (TOPS) mode. $B_\perp$ is perpendicular baseline, B_T is time baseline (day), θ is incidence angle.

conditions in Iran and Iraq (Funning et al. 2005), it was expected that both L-band (ALOS-2) and C-band (Sentinel-1A/B) data can achieve high interferometric coherence.

2.2. *DInSAR measurements*

All Single Look Complex (SLC) data were processed to generate the interferograms using the SARscape software. The Signal-to-Noise Ratio (SNR) of each interferogram was improved by multi-looking the ALOS-2 ScanSAR images with 1 by 5 looks, and Sentinel-1A/B images with 8 by 2 looks, in range and azimuth direction, respectively. For ALOS-2 ScanSAR interferometry, timing and phase compensation at the bounds of bursts and sub-swaths must be conducted in order to avoid phase discontinuities (Guarnieri and Prati 1996). Regarding Sentinel-1A/B TOPS SAR data, co-registration with an accuracy of about 1/1000th of one pixel in the azimuth direction is required due to the Doppler centroid frequency variations caused by azimuth beam sweeping (González et al. 2015). The topographic phases, derived from the 3 arc-second Digital Elevation Model (DEM) from the Shuttle Radar Topography Mission (SRTM) (Farr and Kobrick 2000), were used for removing the topographic effects. Interferograms were subsequently filtered using Goldstein Adaptive Filter (Goldstein and Werner 1998). A linear function, consisting of slant range coordinate (range, azimuth) and error phase was estimated afterwards, with observations on the non-deforming areas to remove the residual phase and orbital error. Once this step was completed, the interferograms were unwrapped using Minimum Cost Flow method (Costantini 1998; Costantini and Rosen 1999), and geocoded to the WGS84 geographic coordinates with 180 m resolution for ALOS-2 ScanSAR pairs, and 30 m resolution for Sentinel-1A/B TOPS pairs (Figure 2).

Two elliptic deformation areas were observed in all the deformation maps. The maximum line-of-sight (LOS) deformation was 91.8 cm and 48.8 cm for ALOS-2 ascending and descending pairs, respectively. As for the DInSAR measurements from the Sentinel-1A/B ascending pair, the deformation pattern was similar to the ALOS-2 ascending result but with a peak deformation of 87.3 cm along the LOS direction. Two Sentinel-1A/B descending deformation maps show similar deformation pattern but with different maximum LOS deformation around the epicentre, 65.0 cm and 54.8 cm for the 6-day and 12-day pairs, respectively. To reduce the number of data points and improve computational efficiency, several million data points in the area between latitude 33.41° N – 36.14° N and longitude 43.78° E – 47.90° E were subsampled using a regular mesh, of higher density around the deforming area. As a result, 51,559 points were obtained, with 19,909 for ALOS-2 and 31,650 for Sentinel-1A/B (Figure 3).

3. Modelling

To further analyse and describe the causative fault for the main shock, all subsampled observations were inverted using a finite dislocation model in an elastic, homogeneous half-space (Okada 1985). Geodetic inversion consisted of two steps: a non-linear inversion was adopted to constrain all the fault parameters with a uniform slip model, followed by a linear inversion to infer slip distribution on the fault plane.

Non-linear inversion, a mix algorithm of Gauss-Newton iteration and gradient descent as the Levenberg-Marquardt (LM) least-squares approach (Marquardt 1963), was applied to constrain 9 fault parameters (namely, length, width, depth, longitude, latitude, strike,

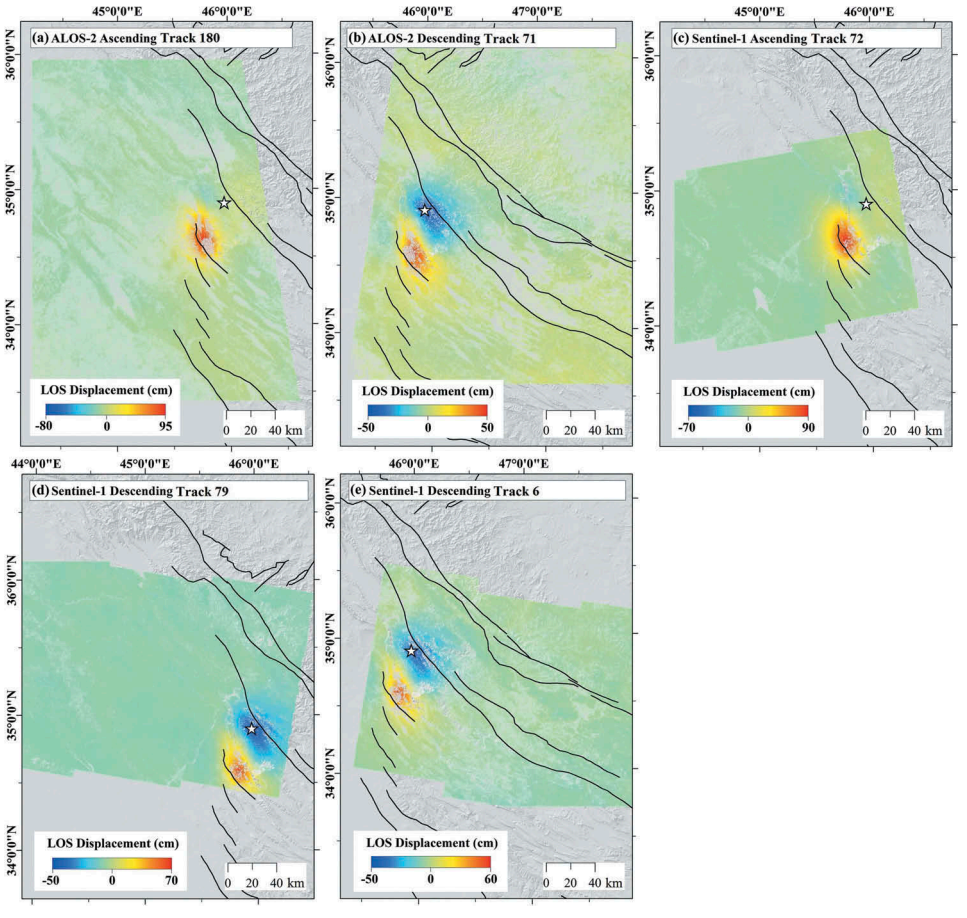

Figure 2. DInSAR measurements (LOS) of the 2017 M_W 7.3 Kermanshah Earthquake. (a)–(b) ALOS-2 ascending and descending displacement maps; (c)–(e) Sentinel-1A/B ascending and descending displacement maps. Red and blue colours represent decrease and increase in the LOS range, respectively. The white star is main shock, and black lines are active faults in western Iran.

dip, rake, and slip) by assuming no dilation between the hanging wall and footwall. A non-linear inversion with multiple random restarts (Atzori et al. 2009), and initial parameters from the Global Centroid Moment Tensor Catalogue (GCMT) solution was applied to search for a global minimum in the optimization process. The cost function applied can be expressed as a weight mean of residuals, as shown in Equation (1):

$$\mathrm{CF} = \sqrt{\frac{1}{N}\sum_{i}^{N}\frac{\left(d_{i,\mathrm{obs}} - d_{i,\mathrm{mod}}\right)^2}{\sigma_i}} \tag{1}$$

Where CF is the residuals estimated from the cost function, $d_{i,\mathrm{obs}}$ and $d_{i,\mathrm{mod}}$ are observed and modelled data corresponding to i^{th} data point, respectively; σ_i is standard deviation for the N points.

In order to retrieve slip distribution on the fault plane, a linear inversion was applied by fixing the fault geometry inverted from non-linear inversion. The length and width of

the fault plane were extended to cover the earthquake's epicentre area. Subsequently, the fault plane was subdivided into small patches along the strike and dip; each patch measuring 5 km× 5 km. To avoid extremely high values or oscillations in the result, a non-negative least-squares algorithm with a damping parameter was introduced into the system, as shown in Equation (2):

$$\begin{bmatrix} \mathbf{d}_{\mathrm{DInSAR}} \\ 0 \end{bmatrix} = \begin{bmatrix} G \\ \varepsilon L^2 \end{bmatrix} \mathbf{m} \tag{2}$$

Where $\mathbf{d}_{\mathrm{DInSAR}}$ is the DInSAR measurements, $\mathbf{m}$ is the slip vector for each patch, G is a matrix containing Green's function with an extended Laplacian operator L^2 which is weighted by an empirical coefficient ε (Wright, Lu, and Wicks 2003). The empirical coefficient ε, also called damping factor, is determined based on the trade-off curve between the misfit of measurement and the solution roughness of slip distribution (Jónsson et al. 2002; Wright, Lu, and Wicks 2004). The solution roughness can be estimated as the mean, absolute Laplacian of the slip distribution (Jónsson et al. 2002), as shown in Equation (3):

$$\rho = \frac{\sum_i |\boldsymbol{P}|}{2S} \tag{3}$$

Where $P = L^2\mathbf{m}$ and S represents the total number of small patches on the fault plane. Changes in values of the damping factor generated different optimal solutions. High values resulted in a large misfit; low values led to small misfit, but with large oscillation in slip distribution. After several trials the damping factor was set to be 0.36 to obtain the best-fitting results; that is, a compromise solution minimising misfit and providing small roughness at the same time (Figure 4). A non-negative least square algorithm was adopted to positively invert this system and increase the reliability of the source model, as suggested by (Atzori and Salvi 2014).

4. Results

4.1. *Separate inversion results using ALOS-2 and sentinel-1A/B ascending and descending data individually*

Firstly, we separately inverted the source model, using ALOS-2 or Sentinel-1A/B ascending and descending data independently. Table 2 shows the source parameter of uniform slip model using different dataset. The source fault models, as constrained by using ALOS-2 ascending and descending measurements separately, show a strike of about 353° and a rake of 140°, though with different dips. Both solutions are dipping NE, with a slightly larger dip (21.9°) for the ALOS-2 ascending inversion, as compared to a dip of 13.5° for the ALOS-2 descending solution. As well, different slip patterns can be identified from the slip distribution, as shown in Figure 5(a,b). A wider concentrated high-slip patch with a magnitude over 1.75 m was retrieved from the slip distribution inversion using ALOS-2 ascending data, with a peak slip of approximately 4 m at a depth of 14 km, much higher than that from ALOS-2 descending inversion. With regard to the source fault model constrained from Sentinel-1A/B ascending and descending measurements separately, strike and rake exhibit results similar to the ALOS-2 data; both solutions implied larger dip angles, with 27.3° and 15.4° for Sentinel-1A/B ascending and

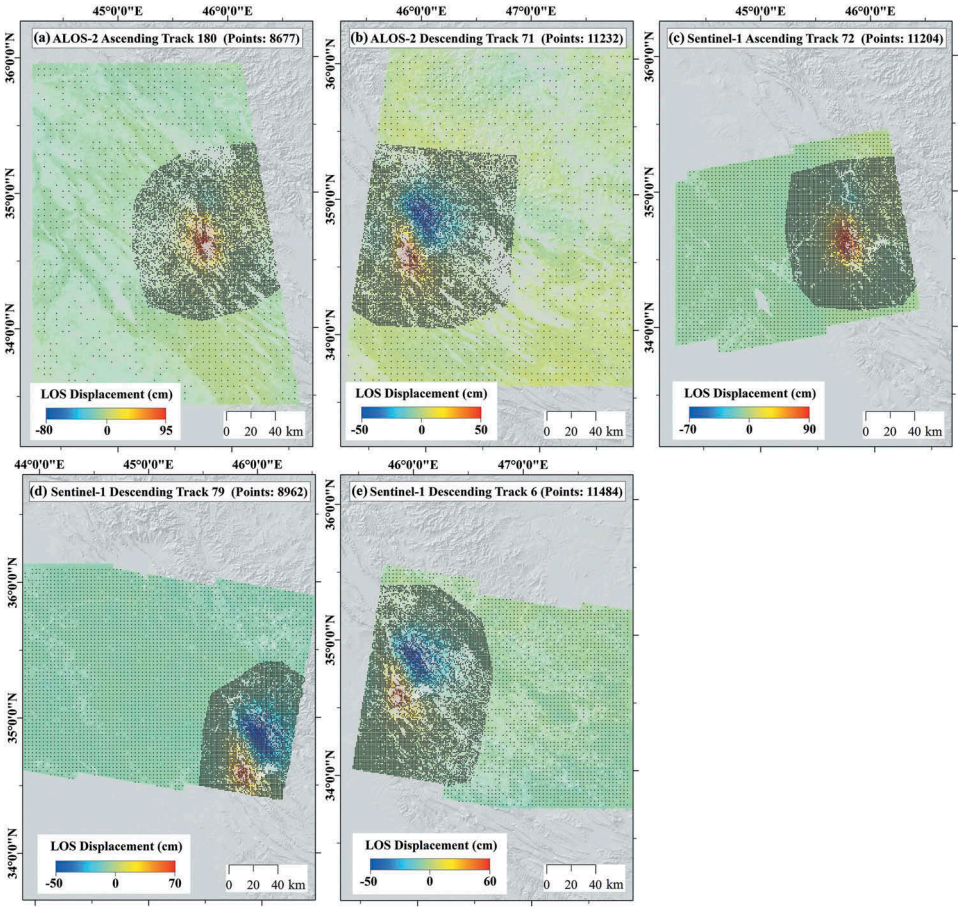

Figure 3. Down-sampled points from five coseismic displacement maps used in this study. (a)–(b) ALOS-2 ascending (Track 180) and descending (Track 71) displacement maps; (c)–(e) Sentinel-1A/B ascending (Track 72) and descending (Track 79 and 6) displacement maps. Red and blue colours represent decrease and increase in the LOS range, respectively.

descending inversion, respectively. Figure 5(d,e) show the slip distributions for Sentinel-1A/B ascending and descending data, respectively. The results evidence a slip pattern similar to the comparison between ALOS-2 ascending and descending inversion, while the peak slip for Sentinel-1A/B descending solution is 3.58 m at a depth of 15 km.

Secondly, we inverted the slip distribution by jointly using ALOS-2 or Sentinel-1A/B ascending and descending data. Both solutions showed similar fault geometries, striking 353° NNW, dipping about 16.0° NE with a rake of ~137°. Figure 5(c,f) shows the inverted slip distributions, as constrained by ALOS-2 and Sentinel-1A/B data, respectively. The slip patterns from both solutions are consistent, suggesting a concentrated slip patch with a magnitude of over 1.0 m at a depth of 10–17 km. However, the peak slip inverted from the ALOS-2 ascending and descending inversion was 3.57 m at a depth of 13 km, which is slightly smaller than the Sentinel-1A/B ascending and descending solution, with a peak slip of 3.76 m at the same depth.

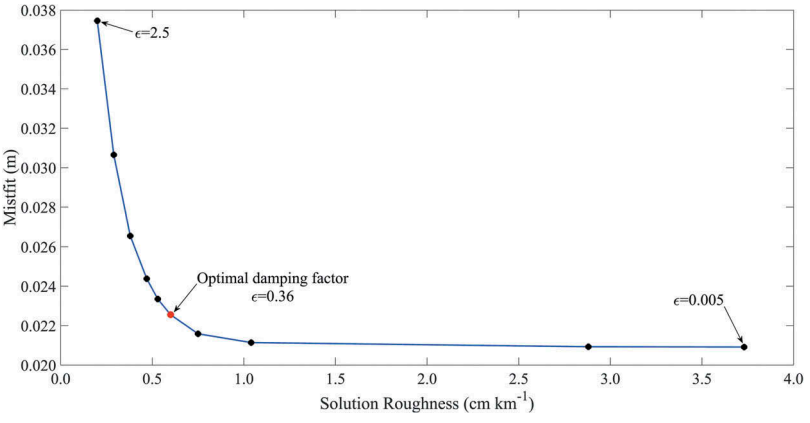

Figure 4. Trade-off curve between the misfit of measurement and the solution roughness for the slip distribution. Each black dot on the curve represents one individual experiment with specific value of damping factor. The red dot is the optimal damping factor with 0.36 we chose in this study.

4.2. *Joint inversion results using both ALOS-2 and sentinel-1A/B data*

A joint inversion using ALOS-2 and Sentinel-1A/B data was implemented to invert the optimized source fault. The best-fit source fault constrained from the uniform slip model shows a reverse fault with a relatively large right-lateral component, striking 353.5° NNW-SSE and dipping 16.3° NE with a depth of 11 km (refer to top edge of the fault plane). The strike, dip, and rake are similar to the solutions reported by the USGS and the GCMT (Table 3). Also, the small NE-dipping angle obtained generally agrees with results from the Geospatial Information Authority of Japan (GSI) (Kobayashi et al. 2017), and previous studies carried out in this region (Vergés et al. 2011; Madanipour et al. 2013). Fixing the fault geometry from the uniform slip model, and extending the fault length and width 100 km along the strike and 80 km along the dip, respectively, resulted in an inverted slip distribution, with a distributed slip model. Likewise, the fault plane was discretized into 320 patches of 5 km × 5 km. Figure 6 shows the slip distribution on the fault plane; with most of the slip occurring at depth between 10 and 17 km, the peak slip appears to have been of 3.87 m at a depth of 13 km. The total inferred seismic moment was estimated at 1.01×10^{20} Nm, corresponding to a moment magnitude of M_W 7.3, which is consistent with results from the USGS, IRSC and ISMN, but slightly smaller than the GCMT (M_W 7.4). The aftershocks (Figure 6(b)) generally appear to be located around the fault plane, indicating a good agreement between fault geometry and aftershock distribution.

Figure 7 shows the residuals from the misfit between DInSAR LOS observations and model data. The small root-mean-square error (RMSE) values from misfit analysis indicate that the observed data were well reproduced for most of the areas. The RMSE values are 2.8 cm, 2.2 cm, 1.9 cm, 1.5 cm, and 2.9 cm for ALOS-2 ascending, ALOS-2 descending, Sentinel-1 ascending, Sentinel-1 descending, and Sentinel-1 12-day descending pairs, respectively. The residual deformation is likely due to secondary coseismic geological disasters (landslides and rockfalls).

Table 2. Source parameters of uniform slip model inverted from different data.

Data	Length (km)	Width (km)	Depth* (km)	Strike (°)	Dip (°)	Longitude** (°)	Latitude** (°)	Rake (°)	Slip (m)
ALOS-2 ASC	38.9	21.8	11.6	353.9	21.9	45.850	34.732	140.8	3.78
ALOS-2 DESC	43.6	17.0	12.4	352.1	13.5	45.861	34.729	139.6	3.35
Sentinel-1 ASC	37.8	19.5	13.6	351.7	27.3	45.835	34.736	143.2	4.60
Sentinel-1 DESC	41.4	15.2	13.2	353.8	15.4	45.858	34.731	141.0	3.85
ALOS-2 ASC and DESC	41.1	21.7	10.6	352.9	16.0	45.861	34.728	136.3	3.04
Sentinel-1 ASC and DESC	40.5	20.2	11.4	353.7	16.6	45.861	34.731	138.4	3.14

* The depth refers to the top centre of the fault plane.
** Centre of the fault plane projected to the surface.

5. Discussion

5.1. *Linear surface ruptures of the 2017 Kermanshah earthquake*

Linear surface ruptures were mapped in the epicentre area from both ALOS-2 and Sentinel-1A/B ascending and descending interferograms, as shown in Figure 8. Large linear phase discontinuities reached tens of kilometres, featured by loss of coherence near the cities of Sarpol Zahab and Darbandikhan. Especially around the village of Sar Cheqa, as shown by the dash violet rectangle in Figure 8(a–d), clear linear features were found away from the epicentre area. High spatial resolution optical images can be used to verify some small deformation, in combination with the SAR images. This study gathered three SuperView-1 images, acquired three days after the main shock, on 16 November 2017, with 0.5 m and 2 m spatial resolution in panchromatic and multi-spectral mode, respectively. The spatial coverage of each image is shown as white boxes in Figure 8(a–d). Image 098 was acquired around the city of Sarpol Zahab, images 097 and 087 jointly cover the city of Darbandikhan, where the Darbandikhan dam is located.

The optimized source fault model indicated that the 2017 Kermanshah Earthquake occurred on a right-lateral reverse fault without obvious surface rupture on the ground. The above-mentioned high spatial resolution SuperView-1 images were used to verify the linear surface features mapped by DInSAR measurements. A SuperView-1 Pan-sharpened image with 0.5 m resolution was generated by merging the panchromatic and multispectral imagery. Linear surface features near the cities of Sarpol Zahab, Darbandihab and Sar Cheqa were investigated (Figure 9). A large area of loss of coherence along the linear features was observed near the city of Sarpol Zahab, shown with a green dashed rectangle in Figure 9(a), corresponding to the same area of the SuperView-1 098 image of Figure 9(b,c). Obvious surface cracks and landslides in both of panchromatic and pan-sharpened images were clearly identified within the same area. The crack traces on the ground are consistent with the linear surface features mapped from DInSAR measurements. Most surface cracks spread in a NNW-SSE direction and the width of crack zone is up to 400 m. The landslides generally expanded downward, along a SW direction, reaching an area of up to 14,488.8 m^2. Two areas near the city of Darbandikhan exhibit phase discontinuity and loss of coherence (green dashed

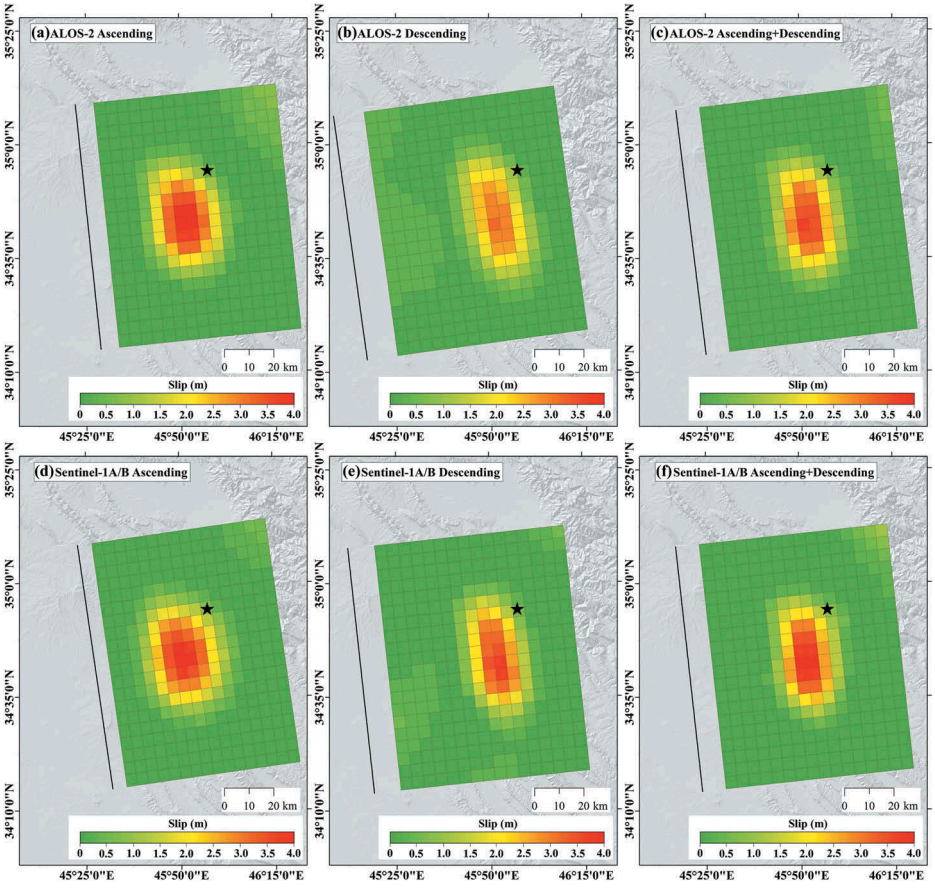

Figure 5. Slip distribution inverted by using (a) ALOS-2 ascending DInSAR measurements (Track 180), (b) ALOS-2 descending DInSAR measurements (Track 71), (c) ALOS-2 ascending and descending DInSAR measurements (Track 180 and 71), (d) Sentinel-1A/B ascending DInSAR measurements (Track 72), (e) Sentinel-1A/B descending DInSAR measurements (Track 79 and 6), (f) Sentinel-1A/B ascending and descending DInSAR measurements (Track 72, 79 and 6). The black star shows the epicentre from USGS and the black lines are corresponding fault traces intersected with the surface.

rectangles in Figure 9(d)). For the area (e) highlighted in Figure 9(d), two significant landslides were identified close to the Darbandikhan Dam, which is a rockfill embankment with a central clay core, as shown in Figure 9(e). Visual interpretation of the pan-sharpened SuperView-1 097 acquired three days after the earthquake (Figure 9(e)), evidence the floodgates of the dam opened to decrease the water level behind the dam. Area (f) highlighted in Figure 9(d), and corresponding to the pan-sharpened SuperView-1 087 image (Figure 9(f)), exhibit several landslides along the road, the largest affecting an area of up to 60,549.9 m^2.

We also found a cluster of linear fringes on ALOS-2 and Sentinel-1A/B ascending and descending interferograms near the village of Sar Cheqa (violet dashed rectangles in Figure 8). Figure 9(g,h) correspond to the same area and show persistence of the cluster over different satellites and time spanning, indicating possible secondary deformation over this area. Owing to the small spatial baseline of ALOS-2 and Sentinel-1A/B

Table 3. Fault parameters of Kermanshah Earthquake from seismology and geodetic inversion.

Source	Length (km)	Width (km)	Depth (km)	Strike (°)	Dip (°)	Longitude (°)	Latitude (°)	Rake (°)	Slip (m)	Seismic Moment (10^{20} Nm)	M_W	Data
USGS			19.0	351.0	16.0	45.956	34.905	137.0		1.12	7.3	
GCMT			16.9	351.0	10.0	45.880	34.790	143.0		1.72	7.4	
IRSC			18.1			45.762	34.772				7.3	
ISMN			18.0			45.910	34.810				7.3	Strong motion
(Kobayashi et al. 2017)	100.0	80.0	3.0		16.0				~ 3.0	1.18	7.3	ALOS-2
Uniform Slip Model	40.7	21.0	11.0*	353.5	16.3	45.862**	34.730**	137.5	3.06	0.79	7.2	ALOS-2, Sentinel-1A/B
Distributed Slip Model	100.0	80.0	2.8*	353.5	16.3	45.865**	34.730**	137.5	3.87	1.01	7.3	ALOS-2, Sentinel-1A/B

* The depth refers to the top centre of the fault plane.
** Centre of the fault plane projected to the surface.

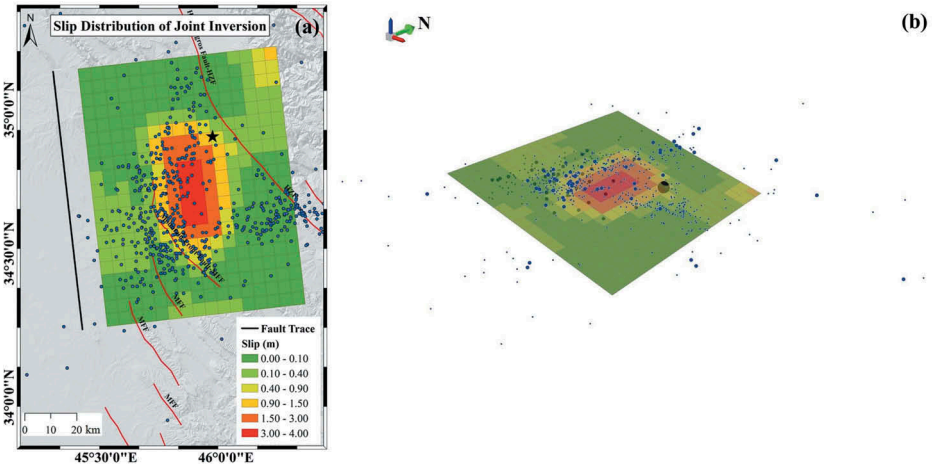

Figure 6. Joint inversion slip distribution using both ALOS-2 and Sentinel-1A/B data for the 2017 M_W 7.3 Kermanshah Earthquake, 2D view of surface projection (a) and 3D view (b). The black star in (a) is main shock, corresponding to the black sphere in (b). Black line is fault trace intersected with the surface. Blue dots in (a-b) are aftershocks, and red lines in (a) are active faults.

interferometric pairs used in this study (Table 1), potential topographic errors or artefacts are unlikely to be responsible for these observed large deformations. An analysis of the area using Google Earth optical imagery (Figure 9(i)), shows that most of the fringes with the linear surface features are located on the slopes of mountains, suggesting high potential for the occurrence of landslides, rockfalls or slump blocks over the area.

Corroboration between DInSAR measurements and the high spatial resolution SuperView-1 images acquired over these three cities suggest that most of the linear surface ruptures mapped by DInSAR could be landslides, cracks or any other triggered gravitational deformation over the epicentre area, rather than secondary fault ruptures. There are other two main reasons to support this conclusion. None of the surface rupture features appears to connect directly to the source fault at depth. Most of them are superficial fractures or landslides rather than fault ruptures on the surface. As well, the topography of steep slopes and rough mountainous landscape dominating this region are supportive of these gravitational deformations.

5.2. *Triggering relationships with neighbouring active faults*

A coseismic slip caused by earthquake is relevant to aftershock distribution and Coulomb stress change on the causative fault and the neighbouring active fault systems. To calculate the stress variation induced by the 2017 Kermanshah Earthquake, we used the inferred distributed slip model as the source, and estimated the stress change on the fault plane itself using a Coulomb Failure Function (Harris 1998). Subsequently, the impact of stress change caused by this earthquake on neighbouring active faults was explored. Based on the Coulomb Failure Function, the stress change on the specific receiver fault is shown as Equation (4):

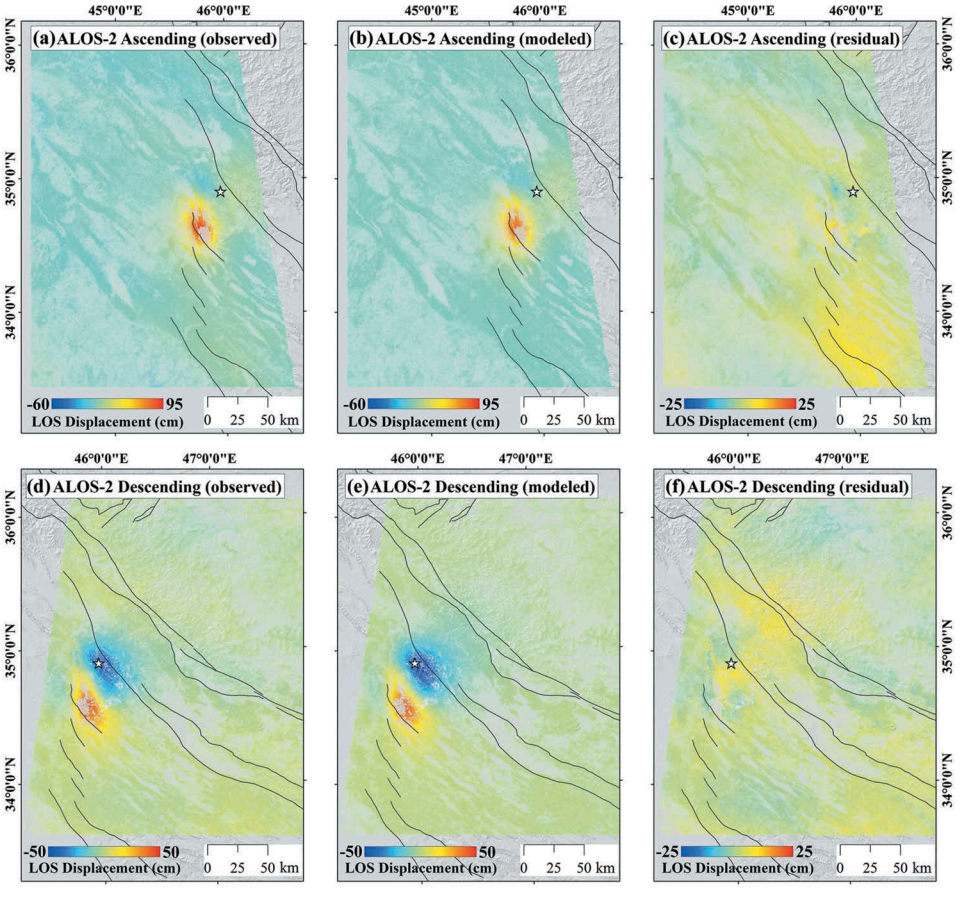

Figure 7. Misfit analysis for the 2017 M_W 7.3 Kermanshah Earthquake. Observed, modelled, and residual data from ALOS-2 ScanSAR ascending (a-c) (Track 180) and descending (d-f) (Track 71), Sentinel-1A/B ascending (g-i) (Track 72), descending (j-l) (Track 79) and descending of 12days (m-o) (Track 6). White star is main shock, and black lines are active faults in western Iran.

$$\Delta\mathrm{CFF} = \Delta\tau + \mu(\Delta\sigma_n - \beta\frac{T}{3}) \tag{4}$$

Where ΔCFF is the stress change estimated from the Coulomb Failure Function, $\Delta\tau$ is the shear stress change, μ is the friction coefficient, $\Delta\sigma_n$ is the normal stress change, β is the Skempton's coefficient and T is the stress tensor trace. Negative Coulomb stress change denotes a decrease in stress, reducing the risk of the failure. Positive Coulomb stress change indicates the stress on the specific fault is increasing, which could further accelerate the failure of the fault. Aftershocks generally occur around the segments of fault plane with positive stress change.

As Equation (4) shows, the friction coefficient μ and shear modulus were set to be 0.4 and 3.0×10^{10} N/m, respectively. Figure 10(a,b) shows the stress change on the source fault plane, with a maximum stress release of up to 7.2 MPa at a depth of 13 km, and a peak stress increase of 2.63 MPa at a depth of 9 km. Positive stress changes mainly occurred at a depth ranging from 7 to 10 km and 15–20 km, where most aftershocks

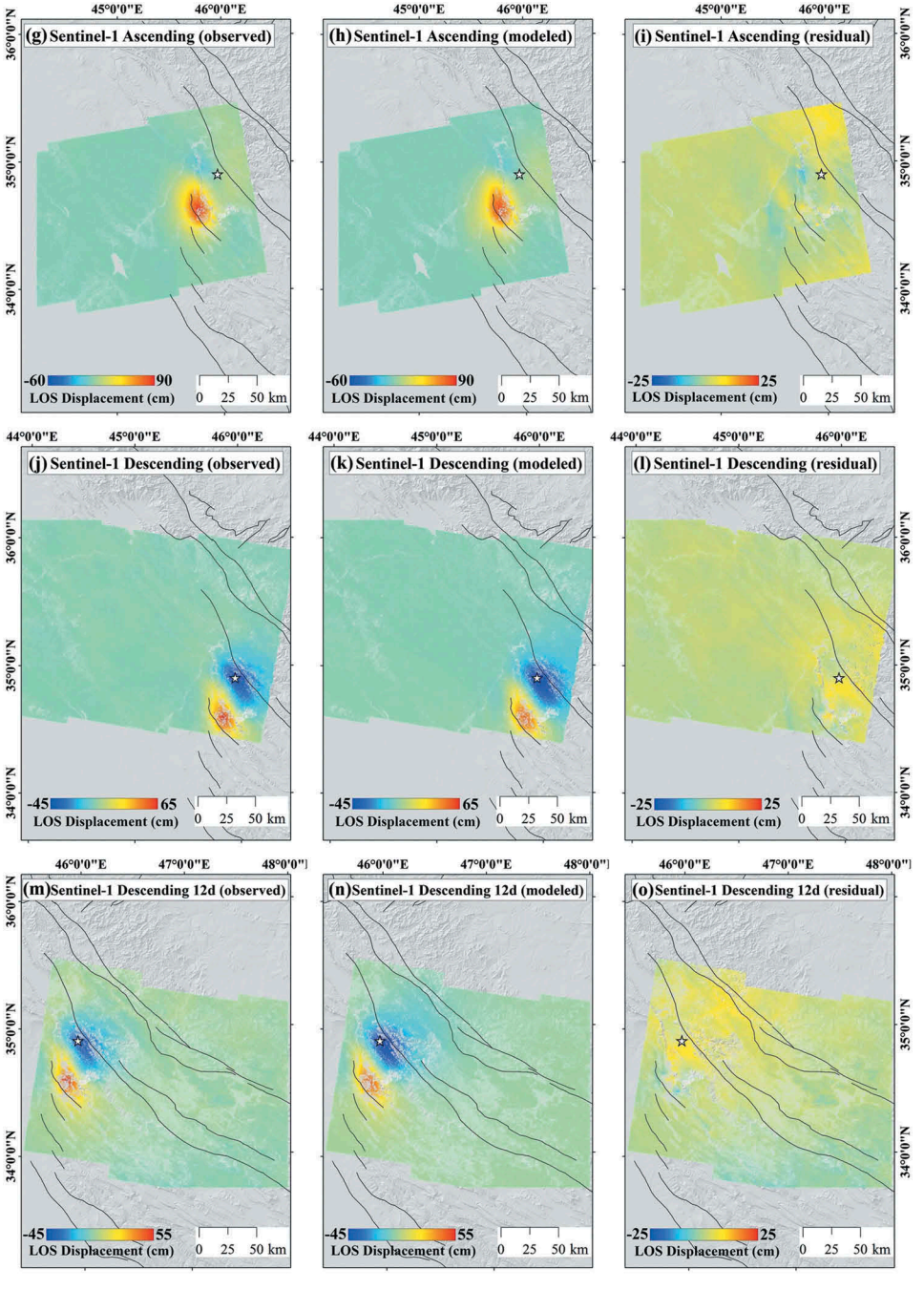

Figure 7. continued.

occurred. On the other hand, stress decrease (negative stress changes) areas were identified at the middle of the source fault plane, coinciding with the occurrence of the main shock. Hence, high loaded stress areas are consistent with the aftershock distribution.

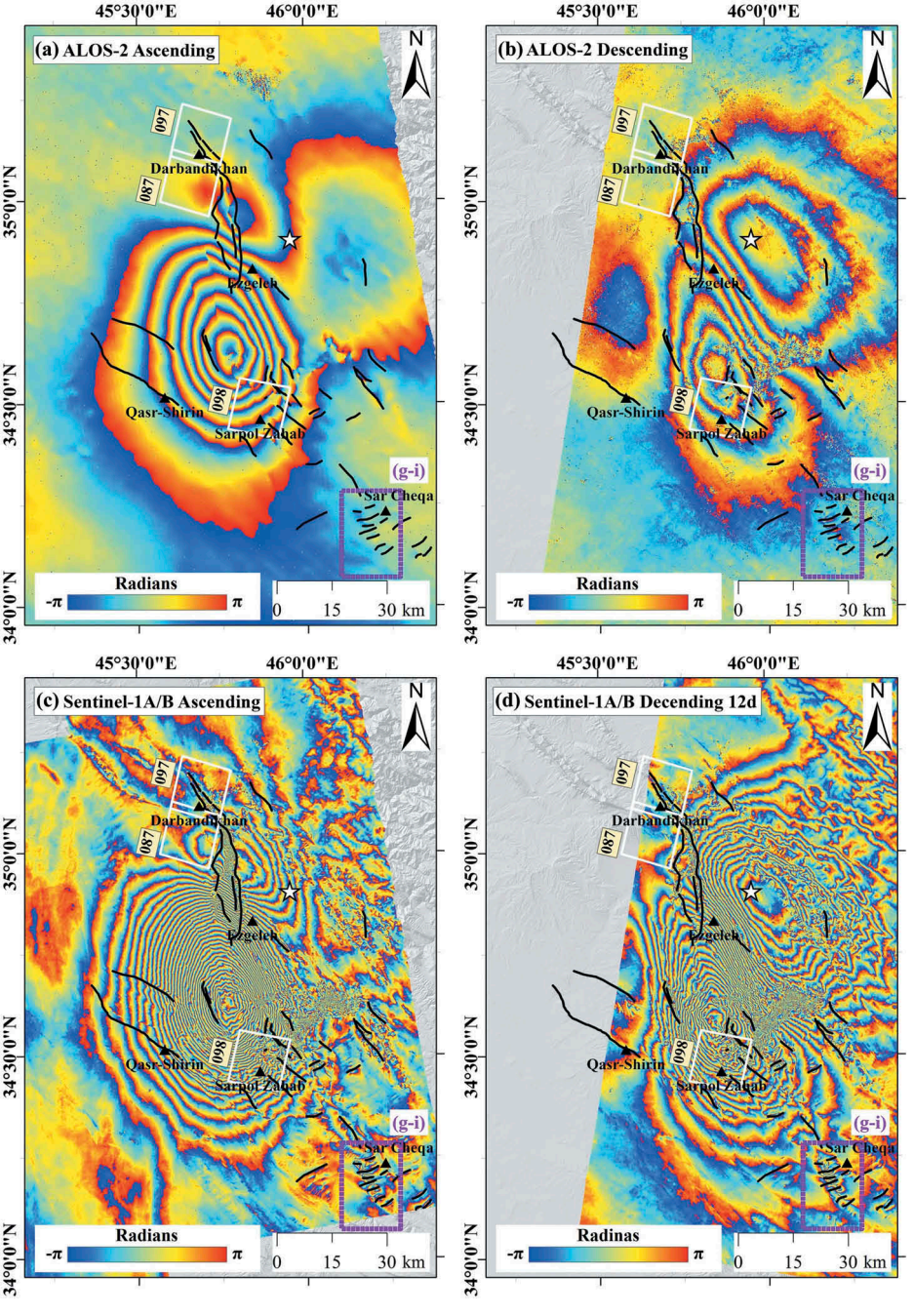

Figure 8. Linear surface ruptures (black lines) identified in (a) ALOS-2 ascending interferogram (Track 180), (b) ALOS-2 descending interferogram (Track 71), (c) Sentinel-1A/B ascending interferogram (Track 72) and (d) Sentinel-1A/B descending interferogram (Track 6). The white star shows the epicentre from USGS and the black triangles are major cities nearby. The white boxes are the footprints of SuperView-1 images. The violet rectangle is the coverage of Figure 9 (g–i).

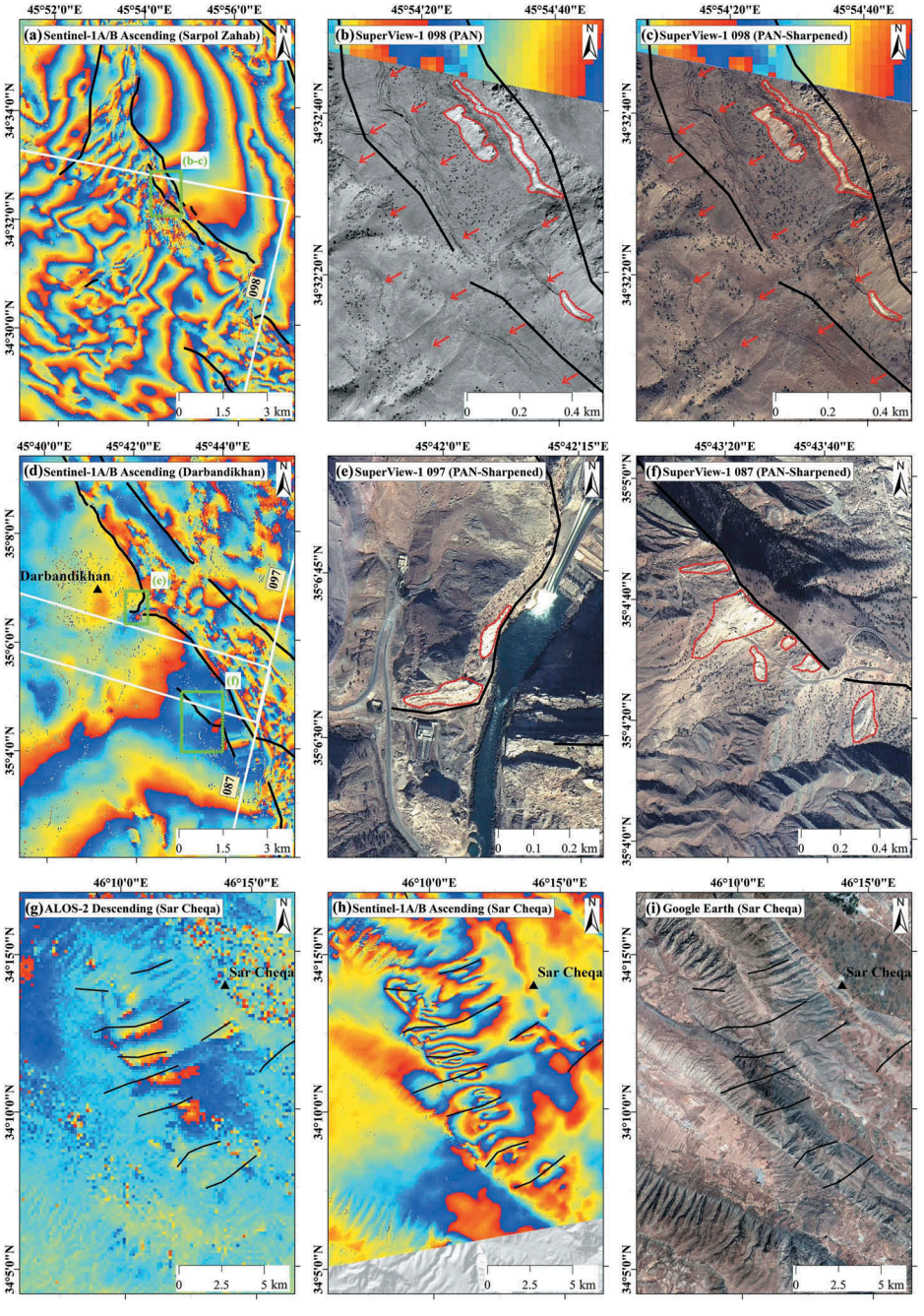

Figure 9. Triggered landslides and surface ruptures near the city of Sarpol Zahab (a–c), Darbandikhan (d–f) and Sar Cheqa (g–i). See Figure 8 for the location of (g–i). The black lines are mapped linear surface ruptures from DInSAR measurements, and the black triangles are major cities or villages. The red arrows show the surface cracks and the red polygons indicate the triggered landslides.

Several active faults observed on, or near, the stress increase areas (Figure 10(a,c)), could be influenced by the 2017 Kermanshah Earthquake. Hence, we further explored the impact that stress changes caused by the earthquake may have had on neighbouring active faults, specifically on the fault plane of the High Zagros Fault (HZF) and the Zagros Mountain Front Fault (MFF), as shown in Figure 10(c). Two fault segments at MFF (MFF-1 and MFF-2) and one fault segment at HZF were adopted as receiver sources in the stress change estimation. The estimated fault geometry of MFF-1, MFF-2, and HZF from a previous study of active faults in Iran (Hessami, Jamali, and Tabassi 2003) was adopted to reconstruct the receiver faults, generally striking NNW and dipping NE 30–60°. It is worth noting that MFF-1, MFF-2 and HZF intersect with the source fault of the Kermanshah Earthquake at a depth of 10 km, 11 km and 18.5 km, respectively. We found a positive stress change on the MFF-1 and MFF-2, and mainly negative stress change on the HZF. The peak positive stress changes on the MFF-1 and MFF-2 were estimated at 3.1 MPa at a depth of 9.5 km, and 1.96 MPa at a depth of 10 km, respectively. High loaded stress areas (>0.5 MPa) on the MFF-1 and MFF-2 are equal to 264 km^2 and 136 km^2, respectively.

Before the 2017 Mw 7.3 Kermanshah Earthquake, only four major earthquakes with over a magnitude of 6.0 occurred on MFF and MRF over the last 50 years; none of which is larger than M_W 7.0, (as shown in Figures 1 and Figure 10(a)). Our inverted source fault model shows the 2017 Kermanshah Earthquake ruptured on a previously unidentified fault, rather than MFF or HZF around the epicentre. However, the proximity among MFF, HZF, and the source fault of this event brought out the question of whether this earthquake could promote or trigger any other earthquake activities on these two major fault systems. Coulomb stress change analysis (Figure 10(*c*)), shows the rupture of the 2017 Kermanshah Earthquake brought 0.5–3.1 MPa and 0.5–1.96 MPa to MFF-1 and MFF-2, closer to failure, respectively. This suggests that the risk of earthquakes on both MFF-1 and MFF-2 is increasing. However, there is more negative stress change imparted to HZF. After collecting major aftershocks ($M_W \geq 5.0$) within 200 km around the epicentre between 12 November 2017 and 11 April 2018 from the IRSC, we found two events occurred on the fault plane of MFF-2; one with M_W 5.0 on 6 January 2018, and the other with M_W 5.3 on 1 April 2018 (shown with green circles in Figure 10(a,c)). Both aftershocks occurred on the segments of MFF-2 that exhibited positive stress changes, which is consistent with the Coulomb stress analysis undertaken in this study. Thus, it appears that the risk of seismic hazard on MFF-1 keeps increasing, while it is likely that the major aftershocks on MFF-2 reduced the chance of fault failure.

Moreover, we found a series of events with a magnitude over M_W 5.0 occurred on the ZFF on 11 January 2018, with a peak magnitude of 5.6, shown by the green circles in Figure 10(a,d). These major events were followed by a cluster of small events ($2.5 \leq M_W < 5.0$) that occurred over the same region. Owing to the nearly parallel location between MFF and ZFF, we also explored the Coulomb stress change on these faults using the estimated geometry (Hessami, Jamali, and Tabassi 2003) to evaluate their risk of failure. Figure 10(d) shows only a few segments with small stress increase (≤0.5 MPa) on MFF-3, MFF-4, MFF-5, and ZFF. Also, the negative stress change dominates the fault planes of MFF-3, MFF-4, MFF-5, and ZFF, suggesting that the 2017 Kermanshah Earthquake is likely to inhibit the failure of these four active faults. Fewer aftershocks were observed between the source fault of the 2017 Kermanshah Earthquake and ZFF,

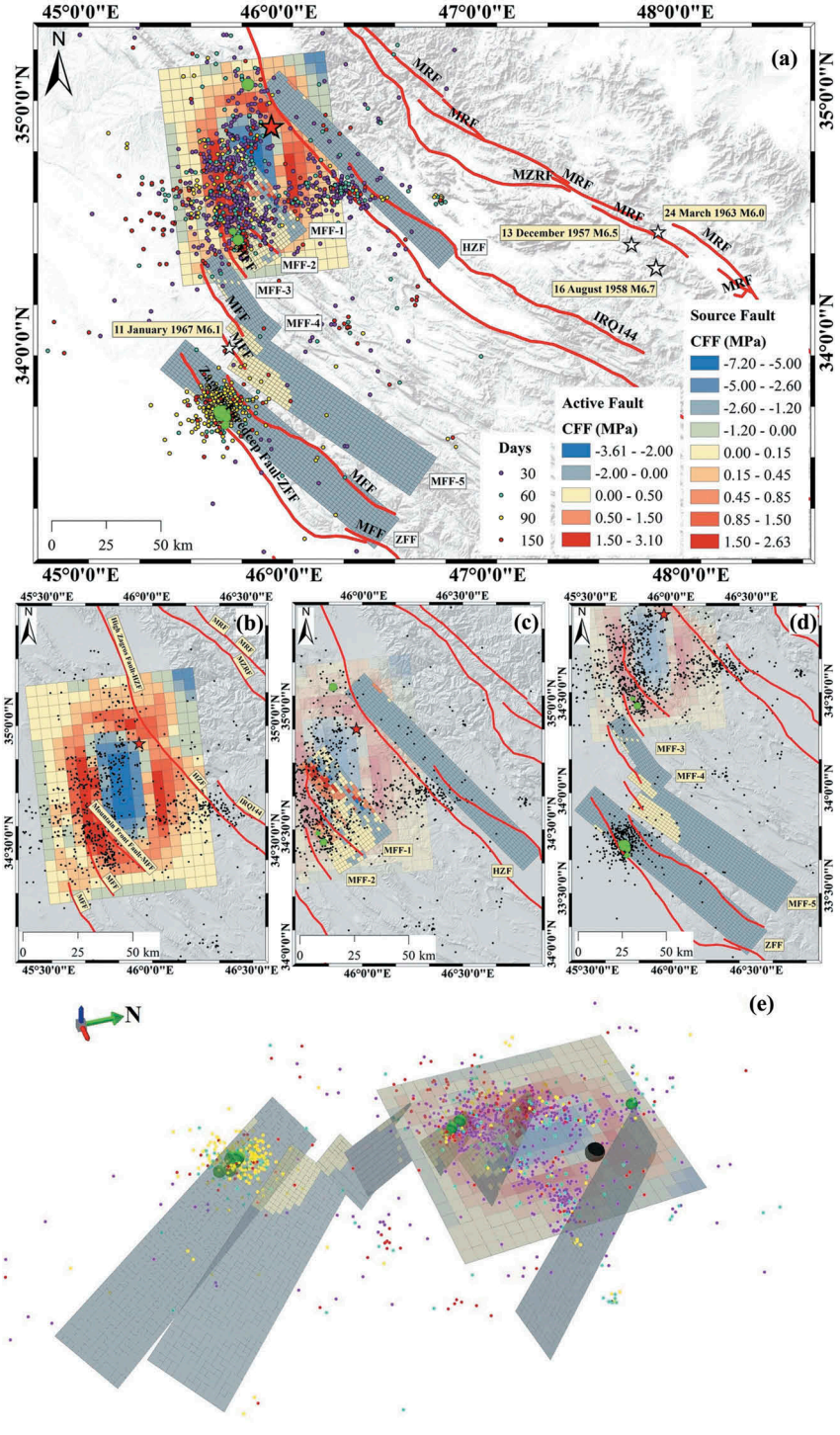

Figure 10. (a) Coulomb stress change on the source fault plane of the 2017 M_W 7.3 Kermanshah Earthquake and the neighbouring active faults investigated in this study. White stars are major historical earthquakes in this region. The small dots with different colours are aftershocks occurred within 150 days after main shock, same as the black dots in (b-d). Enlarged maps for (b) source plane; (c) MFF-1, MFF-2, HZF; (d) MFF-3, MFF-4, MFF-5, and ZFF. (e) The 3D view for source fault and active fault planes. The red star in (a-d) shows the main shock, corresponding to the black sphere in (e). Green circles in (a–e) show the location of major aftershocks (M_W≥5.0). Red lines are active faults.

where MFF-3, MFF-4 and MFF-5 are located (Figure 10(a,e)); hence it is likely these major events and the following small quakes are not related to the aftershocks triggered by the 2017 Kermanshah Earthquake. Even though aftershocks following the main shock could occur within the distance one or two times of rupture length from source fault, these major events occurred on ZFF should be classified as new events on various sources, unrelated to the aftershocks.

6. Concluding remarks

This study used ALOS-2 ScanSAR and Sentinel-1A/B TOPSAR ascending and descending data to map the coseismic deformation of the 2017 M_W 7.3 Kermanshah Earthquake. The low-vegetation coverage and desert-like condition enabled DInSAR measurements maintain a high level of coherence over most parts of the region. Many linear surface features were detected from both ascending and descending wrapped interferograms. The maximum LOS deformation measured from DInSAR was up to 90 cm. Using the DInSAR measurements, source parameters, and slip distribution of the 2017 Kermanshah Earthquake were determined by a joint inversion. The results indicate a blind reverse fault striking 353.5° NNW-SSE and dipping 16.3° NE with a large right-lateral component. The peak slip was up to 3.87 m at a depth of 13 km. The results of joint inversion are consistent with seismological solutions and published results from the Geospatial Information Authority of Japan (GSI) using ALOS-2 data (Kobayashi et al. 2017). The calculation of Coulomb stress change on the source fault and neighbouring active faults evidences high loaded stress change on the source plane, consistent with aftershock distribution. Most importantly, we found that the stress increase on two segments of the Zagros Mountain Front Fault (MFF), MFF-1 and MFF-2, are relatively high and cover a large area on the fault plane. This may promote or even trigger earthquake activities over both segments of fault. However, the following major aftershocks with a magnitude over 5.0 occurred on MFF-2, suggesting that the risk of seismic hazard on this fault has decreased, but MFF-1 might still be brought closer to failure owing to stress increase. Stress decrease dominated on ZFF, indicating that most recent major events with over M_W 5.0 on this fault are not related to aftershocks following the 2017 Kermanshah Earthquake. Comparison between DInSAR measurements and high spatial resolution optical images from SuperView-1 suggest that most linear surface ruptures are likely landslides, ground cracks or rockfalls that occurred around the epicentre area.

Acknowledgments

The ALOS-2 ScanSAR data are provided by the Japan Aerospace Exploration Agency (JAXA) and the Sentinel-1 SAR data are provided by the European Space Agency (ESA). The information about aftershocks is provided by Iranian Seismological Centre (IRSC). The details on active faults are provided by the International Institute of Earthquake Engineering and Seismology (IIEES) in Iran. We thank Space View for making SuperView-1 postseismic images publicly available. The first author gratefully acknowledges financial support from the China Scholarship Council (CSC). This research was partly supported under the Australian Research Council's Discovery funding scheme (project number DP130101694) and JAXA PI investigation project 1419 – Automated

interferometric analysis of L-band SAR satellite data for operational earthquake and volcano monitoring.

Authors' contribution

Linin Ge and Graciela Isabel Metternicht proposed the topic and evaluated the accuracy of the results, Jianming Kuang performed the entire analysis and wrote the manuscript, Alex Hay-Man Ng helped with the DInSAR analysis, Hua Wang helped with the modelling analysis, and Mehdi Zare and Farnaz Kamranzad helped with data collection and manuscript preparation.

Disclosure statement

No potential conflict of interest was reported by the authors.

Funding

This work was supported by the Australian Research Council [DP130101694];China Scholarship Council [201608440352].

ORCID

Linlin Ge http://orcid.org/0000-0001-9275-7980

References

Ambraseys, N., A. Moinfar, and P. Peronaci. 1973. "The Seismieity of Iran the Farsinaj (Kermanshah) Earthquake of 13 Decemher 1957." *Annals of Geophysics* 26 (4): 679–692.

Atzori, S., I. Hunstad, M. Chini, S. Salvi, C. Tolomei, C. Bignami, S. Stramondo, E. Trasatti, A. Antonioli, and E. Boschi. 2009. "Finite Fault Inversion of DInSAR Coseismic Displacement of the 2009 L'Aquila Earthquake (Central Italy)." *Geophysical Research Letters* 36 (15): L15305. doi:10.1029/2009gl039293.

Atzori, S., and S. Salvi. 2014. "SAR Data Analysis in Solid Earth Geophysics: From Science to Risk Management." In *Land Applications of Radar Remote Sensing*, 2–43. Rijeka, Croatia: InTech.

Berberian, M., M. Qorashi, J. A. Jackson, K. Priestley, and T. Wallace. 1992. "The Rudbar-Tarom Earthquake of 20 June 1990 in NW Persia: Preliminary Field and Seismological Observations, and Its Tectonic Significance." *Bulletin of the Seismological Society of America* 82 (4): 1726–1755.

Costantini, M., and P. A. Rosen. 1999. "A Generalized Phase Unwrapping Approach for Sparse Data." Paper presented at the Geoscience and Remote Sensing Symposium, 1999. IGARSS'99 Proceedings. IEEE 1999 International, 267–269.

Costantini, M. 1998. "A Novel Phase Unwrapping Method Based on Network Programming." *IEEE Transactions on Geoscience and Remote Sensing* 36 (3): 813–821. doi:10.1109/36.673674.

De Zan, F., and A. M. Monti Guarnieri. 2006. "TOPSAR: Terrain Observation by Progressive Scans." *IEEE Transactions on Geoscience and Remote Sensing* 44 (9): 2352–2360. doi:10.1109/TGRS.2006.873853.

Dziewonski, A. M., T. -. A. Chou, and J. H. Woodhouse. 1981. "Determination of Earthquake Source Parameters from Waveform Data for Studies of Global and Regional Seismicity." *Journal of Geophysical Research: Solid Earth* 86 (B4): 2825–2852. doi:10.1029/JB086iB04p02825.

Farr, T. G., and M. Kobrick. 2000. The Shuttle Radar Topography Mission. Paper presented at the RTO SET Symposium on Space-Based Observation Technology, Island of Samos, Greece, October 16–18 and published in RTO MP-61. Pasadena, Ca: Jet Propulsion Lab.

Farzanegan, E., M. P. Shahvar, A. Eshaghi, M. Mirsanjari, H. Abdollahi, and H. M. Alavijeh. 2017. "Report of the November 12, 2017 Sarpol-E Zahab, Kermanshah Province Earthquake." In *Iran Strong Motion Network (ISMN)*. Tehran, Iran: Road, Housing & Urban Development Research Center (BHRC).

Funning, G. J., B. Parsons, T. J. Wright, J. A. Jackson, and E. J. Fielding. 2005. "Surface Displacements and Source Parameters of the 2003 Bam (Iran) Earthquake from Envisat Advanced Synthetic Aperture Radar Imagery." *Journal of Geophysical Research: Solid Earth* 110 (B9): B09406. doi:10.1029/2004JB003338.

Goldstein, R. M., and C. L. Werner. 1998. "Radar Interferogram Filtering for Geophysical Applications." *Geophysical Research Letters* 25 (21): 4035–4038. doi:10.1029/1998GL900033.

González, P. J., M. Bagnardi, A. J. Hooper, Y. Larsen, P. Marinkovic, S. V. Samsonov, and T. J. Wright. 2015. "The 2014–2015 Eruption of Fogo Volcano: Geodetic Modeling of Sentinel-1 TOPS Interferometry." *Geophysical Research Letters* 42 (21): 9239–9246. doi:10.1002/2015GL066003.

Guarnieri, A. M., and C. Prati. 1996. "ScanSAR Focusing and Interferometry." *IEEE Transactions on Geoscience and Remote Sensing* 34 (4): 1029–1038. doi:10.1109/36.508420.

Harris, R. A. 1998. "Introduction to Special Section: Stress Triggers, Stress Shadows, and Implications for Seismic Hazard." *Journal of Geophysical Research: Solid Earth* 103 (B10): 24347–24358. doi:10.1029/98JB01576.

Hessami, K., F. Jamali, and H. Tabassi. 2003. *Major Active Faults of Iran*. Tehran, Iran: International Institute of Earthquake Engineering and Seismology.

Jónsson, S., H. Zebker, P. Segall, and F. Amelung. 2002. "Fault Slip Distribution of the 1999 Mw 7.1 Hector Mine, California, Earthquake, Estimated from Satellite Radar and GPS Measurements." *Bulletin of the Seismological Society of America* 92 (4): 1377–1389. doi:10.1785/0120000922.

Kobayashi, T., Y. Morishita, H. Yarai, and S. Fujiwara. 2017. "InSAR-derived Crustal Deformation and Reverse Fault Motion of the 2017 Iran-Iraq Earthquake in the Northwestern Part of the Zagros Orogenic Belt." Sunnyvale, CA: Bull. Geospatial Info.

Kreemer, C., G. Blewitt, and E. C. Klein. 2014. "A Geodetic Plate Motion and Global Strain Rate Model." *Geochemistry, Geophysics, Geosystems* 15 (10): 3849–3889.

Madanipour, S., T. A. Ehlers, A. Yassaghi, M. Rezaeian, E. Enkelmann, and A. Bahroudi. 2013. "Synchronous Deformation on Orogenic Plateau Margins: Insights from the Arabia–Eurasia Collision." *Tectonophysics* 608: 440–451. doi:10.1016/j.tecto.2013.09.003.

Marquardt, D. W. 1963. "An Algorithm for Least-Squares Estimation of Nonlinear Parameters." *Journal of the Society for Industrial and Applied Mathematics* 11 (2): 431–441. doi:10.1137/0111030.

McQuarrie, N. 2004. "Crustal Scale Geometry of the Zagros Fold–Thrust Belt, Iran." *Journal of Structural Geology* 26 (3): 519–535. doi:10.1016/j.jsg.2003.08.009.

Mouthereau, F., O. Lacombe, and J. Vergés. 2012. "Building the Zagros Collisional Orogen: Timing, Strain Distribution and the Dynamics of Arabia/Eurasia Plate Convergence." *Tectonophysics* 532: 27–60. doi:10.1016/j.tecto.2012.01.022.

Okada, Y. 1985. "Surface Deformation Due to Shear and Tensile Faults in a Half-Space." *Bulletin of the Seismological Society of America* 75 (4): 1135–1154.

Reilinger, R. E., S. C. McClusky, M. B. Oral, R. W. King, M. N. Toksoz, A. A. Barka, I. Kinik, O. Lenk, and I. Sanli. 1997. "Global Positioning System Measurements of Present-Day Crustal Movements in the Arabia-Africa-Eurasia Plate Collision Zone." *Journal of Geophysical Research: Solid Earth* 102 (B5): 9983–9999. doi:10.1029/96JB03736.

Shahryar Solaymani Azad, N., S. M. Moradi, A. Ajhdari, T. Youssefi, M. Mashal, and M. Roustaie. 2017. *Preliminary Report on Geological Features of the Ezgaleh-Kermanshah Earthquake*. Tehran, Iran: Geological Survey of Iran Seismotectonics & Seismology Department.

Torres, R., P. Snoeij, D. Geudtner, D. Bibby, M. Davidson, E. Attema, P. Potin, B. Rommen, N. Floury, and M. Brown. 2012. "GMES Sentinel-1 Mission." *Remote Sensing of Environment* 120: 9–24. doi:10.1016/j.rse.2011.05.028.

United States Geological Survey. 2017. "M 7.3 - Iran/Iraq Border." Accessed December 25 2017. https://www.usgs.gov/news/magnitude-73-earthquake-iraniraq-border.

Vergés, J., E. Saura, E. Casciello, M. Fernàndez, A. Villaseñor, I. Jiménez-Munt, and D. García-Castellanos. 2011. "Crustal-Scale Cross-Sections across the NW Zagros Belt: Implications for

the Arabian Margin Reconstruction." *Geological Magazine* 148 (5–6): 739–761. doi:10.1017/S0016756811000331.

Wright, T. J., Z. Lu, and C. Wicks. 2003. "Source Model for the Mw 6.7, 23 October 2002, Nenana Mountain Earthquake (Alaska) from InSAR." *Geophysical Research Letters* 30 (18): 1974. doi:10.1029/2003GL018014.

Wright, T. J., Z. Lu, and C. Wicks. 2004. "Constraining the Slip Distribution and Fault Geometry of the Mw 7.9, 3 November 2002, Denali Fault Earthquake with Interferometric Synthetic Aperture Radar and Global Positioning System Data." *Bulletin of the Seismological Society of America* 94 (6B): S175–S89. doi:10.1785/0120040623.

Zare, M., F. Kamranzad, I. Parcharidis, and V. Tsironi. 2017. Preliminary Report of Mw7.3 Sarpol-E Zahab, Iran Earthquake on November 12, 2017. Tehran, Iran: International Institute of Earthquake Engineering and Seismology (IIEES).